Improved Model-Free Predictive Current Control for Synchronous Reluctance Motor Drives

Cheng-Kai Lin, Jen-te Yu, Yen-Shin Lai, *Fellow, IEEE*, and Hsing-Cheng Yu, *Member, IEEE*

***Abstract*—An improved model-free predictive current control (IMFPCC) method for synchronous reluctance motor (SynRM) drives is presented in this paper. The main advantages of previous MFPCC are that it does not require specific SynRM models and it requires neither motor parameters nor back-EMF estimations. However, this approach has two disadvantages: 1) two current measurements are required in each sampling period, which may lead to the detection of undesirable current spikes caused by instantaneous switching inside the inverter, and 2) an unresolved problem of stagnant current-variation updates, which undermines the prediction performance. This paper intends to eliminate these two drawbacks while retaining all the merits of MFPCC. The proposed IMFPCC is simple and easy to realize. Furthermore, no pulsewidth modulation (PWM) technique is required. A 32-bit microprocessor, TMS320F2809, is utilized to implement both the proposed IMFPCC and the model-based predictive current control (MBPCC) for a performance comparison. Experiment results are provided to validate the proposed method and verify its feasibility.**

***Index Terms*—Predictive current control, six-switch three-phase inverter, synchronous reluctance motor (SynRM).**

I. Introduction

In RECENT years, rugged and simple-structured synchronous reluctance motors (SynRMs) have been widely used in industrial applications and commercial products such as air conditioners, washing machines, and electric vehicles. In general, the SynRMs do not require magnetic materials on their rotors. Compared to the interior permanent-magnet synchronous motor (IPMSM), the SynRM can generate only a reluctance torque, but not an electromagnetic torque. To garner good performance, the inverter used in the current-loop of a SynRM drive system needs to be effectively controlled. Three well-known switching strategies are widely used to control the stator currents of the SynRM. They are hysteresis current control [1], pulsewidth modulation (PWM) [2], and space-vector PWM (SVPWM) [3]. However, none of these three methods can be used to predict the future stator current because of their limitations in nature. On the other hand, model-based predictive current control (MBPCC) is suitable for this purpose, and it has been successfully applied to inverters [4]–[7]. In [4], the authors compared MBPCC and SVPWM.

In [5], a classic study based on a two-level voltage-source inverter was presented, and the author used MBPCC to control the load current. This method involved the decoupled discrete-time model of a balanced three-phase load and its parameters to predict the future load currents corresponding to all possible switching states. Their experiments showed that the method could effectively control the load current if the used parameters of the controller exactly match the real ones. Another method, which was presented in [6] for time-delay compensation, can be used in many MBPCC applications. Furthermore, a digital predictive current controller with 16 switching states, proposed in [7], was successfully implemented on a three-phase two-level four-leg inverter. This method eliminates the PWM-based current controller.

The MBPCC is applicable not only to inverters, but also to converters [8]–[11]. For example, Sanchez *et al.* realized a model PCC for a power converter, and obtained fast and good current-tracking performance [8]. Scoltock *et al.* proposed a model predictive direct current control for a medium-voltage neutral-point-clamped converter with an *LCL*-filter-based connection to the grid [9]. By empirically tuning the controller parameters, they obtained excellent performance. However, the mismatch problem, i.e., the discrepancies between the used parameters and their corresponding true values in the physical system, still has not been effectively resolved. Rivera *et al.* [10] discovered that the predictive-control technique may be an alternative to conventional PWM-based methods to regulate the current of an indirect matrix converter. The current prediction was unsatisfactory because of system model errors.

With the exception of converters, the MBPCC method has also been applied to many kinds of motors, including induction machines [12], segment-winding PM linear SMs [13], PMSMs [14], brushless dc (BLDC) motors [15], [16], IPMSMs [17], and flux-switching PMSMs [18]. For example, Guzman *et al.* proposed a fault-tolerant PCC [19], where the mathematical model of a five-phase induction motor in discrete-time was used to predict future currents. Following the predictive future current and based on the minimization of a cost function, an optimal conducting mode would then be selected and directly applied to the five-phase drive in the next sampling period.

Manuscript received June 3, 2015; revised October 26, 2015 and December 21, 2015; accepted January 9, 2016. Date of publication February 11, 2016; date of current version May 10, 2016. This work was supported in part by the Ministry of Science and Technology of Taiwan, in part by National Taiwan University, in part by National Taipei University of Technology, and in part by National Taiwan Ocean University under Grant MOST 105-2623-E-019-002-ET, Grant MOST 104-2221-E-019-013, and Grant USTP-NTUT-NTOU-104-01.

C.-K. Lin and H.-C. Yu are with National Taiwan Ocean University, Keelung 202, Taiwan (e-mail: cklin@mail.ntou.edu.tw; hcyu@ntou.edu.tw).

J.-t. Yu is with National Taiwan University, Taipei 10617, Taiwan (e-mail: jenteyu@hotmail.com).

Y.-S. Lai is with National Taipei University of Technology, Taipei 106, Taiwan (e-mail: yslai@ntut.edu.tw).

Color versions of one or more of the figures in this paper are available online at http://ieeexplore.ieee.org.

Digital Object Identifier 10.1109/TIE.2016.2527629

Cortes *et al.* [20] have also reported different predictive control methods that were applied to power electronics and drives.

To our best knowledge, there are only a few papers reporting the applications of PCC to SynRMs. The latter motivates this study, which aims at providing an effective solution to the current control of SynRMs.

The traditional three-phase model of SynRMs is essentially a coupling model to which the MBPCCs presented in [5] and [6] are not applicable because of the mutual inductances. To address this modeling problem, the authors of [21] proposed an alternative three-phase model with extended back-EMFs such that the well-known MBPCC [5] may be applied directly. However, only numerical simulation results were provided in that study. Theoretically, the MBPCC [5] can provide good current-tracking performance. Unfortunately, this method still has some limitations including the knowledge of motor parameters, back-EMF estimations, and usage of stator voltages. To eliminate these limitations, an improved model-free predictive current control (IMFPCC) is proposed in this paper. Similar to the MBPCC [5], an optimal conducting mode that minimizes a cost function will be directly applied to the SynRM drive system in the next sampling period. Note that both the MBPCC and the IMFPCC do not require any PWM-based control and its proportional-integral (PI) regulator. However, the MBPCC needs to know the motor parameters in order to predict the future stator current, whereas the IMFPCC does not.

As IMFPCC is based on current measurements and computed current variations, this method is intrinsically insensitive to motor parameter variations and back-EMFs. In IMFPCC, the stator current is measured only once in each sampling period, rather than twice [17], which greatly simplifies the implementation. It is expected that this contribution will be beneficial to various sectors of industry. Based on the information of the measured stator currents and the computed current variations, the future stator currents for all possible conducting modes generated by the inverter can be predicted easily using the addition operation. Thus, low computational load can be achieved, which further implies the burden reduction on the microcontroller. A SynRM drive system equipped with a 32-bit microprocessor TMS320F2809 is built, on which both the MBPCC and the IMFPCC are realized to compare their performances.

Note that a model-free predictive current control (MFPCC) method was presented in [17] for IPMSM. There are two drawbacks exist in the latter. The first one is that it requires two current measurements in each sampling period leading to the detection of current spikes. The second one involves a problem of stagnant current-variation updates. That is, the value of current variation corresponding to one conducting mode is not refreshed during several dozens of time intervals undermining current prediction performance.

The IMFPCC presented in this paper aims at eliminating these two drawbacks. Instead of two current measurements, only one would be needed in each sampling period without the problem of detecting current spikes. In addition to that, a new solution for stagnant current-variation updates would be proposed to resolve the second problem enhancing the current prediction performance.

This paper is organized as follows. Section II presents the equivalent mathematical model of SynRM. The MBPCC is introduced in Section III. The IMFPCC is proposed in Section IV. In Sections V and VI, simulation and experimental results are given to validate the proposed method and verify its feasibility. Finally, conclusion is provided in Section VII.

II. Equivalent Mathematical Model of SynRM

Three equivalent-stator voltage equations of SynRM in the a-b-c stationary reference frame can be expressed in continuous-time as [22], [23]

$$v_a = r_s i_a + \frac{d}{dt}\left(L_q i_a + L_{\mathrm{AA}} i_a + L_{\mathrm{AB}} i_b + L_{\mathrm{AC}} i_c\right) \quad (1)$$

$$v_b = r_s i_b + \frac{d}{dt}\left(L_{\mathrm{BA}} i_a + L_q i_b + L_{\mathrm{BB}} i_b + L_{\mathrm{BC}} i_c\right) \quad (2)$$

$$v_c = r_s i_c + \frac{d}{dt}\left(L_{\mathrm{CA}} i_a + L_{\mathrm{CB}} i_b + L_{\mathrm{CC}} i_c + L_q i_c\right) \quad (3)$$

where r_s represents the stator resistance, L_q denotes the q-axis inductance, v_a, v_b, and v_c are the three-phase stator voltages, i_a, i_b, and i_c are the three-phase stator currents, and $L_{\mathrm{AA}}, L_{\mathrm{AB}}, L_{\mathrm{AC}}, L_{\mathrm{BA}}, L_{\mathrm{BB}}, L_{\mathrm{BC}}, L_{\mathrm{CA}}, L_{\mathrm{CB}}$, and L_{CC} are stator inductances. These inductances, which are relevant to the electrical rotor position of the SynRM, can be classified as self-inductances and mutual inductances. The self-inductances in (1)–(3) can be further written as

$$L_{\mathrm{AA}} = -\frac{1}{2}L_A + \frac{3}{2}L_B + L_B\cos\left(2\theta_{re}\right) \quad (4)$$

$$L_{\mathrm{BB}} = -\frac{1}{2}L_A + \frac{3}{2}L_B - 2L_B\cos\left(2\theta_{re}\right) - \sqrt{3}L_B\sin\left(2\theta_{re}\right) \quad (5)$$

$$L_{\mathrm{CC}} = -\frac{1}{2}L_A + \frac{3}{2}L_B - 2L_B\cos\left(2\theta_{re}\right) + \sqrt{3}L_B\sin\left(2\theta_{re}\right). \quad (6)$$

In addition, the mutual inductances in (1)–(3) can be expressed as

$$L_{\mathrm{AB}} = L_{\mathrm{CB}} = -\frac{1}{2}L_A + L_B\cos\left(2\theta_{re} - \frac{2\pi}{3}\right) \quad (7)$$

$$L_{\mathrm{AC}} = L_{\mathrm{BC}} = -\frac{1}{2}L_A + L_B\cos\left(2\theta_{re} + \frac{2\pi}{3}\right) \quad (8)$$

$$L_{\mathrm{BA}} = L_{\mathrm{CA}} = -\frac{1}{2}L_A - 2L_B\cos\left(2\theta_{re}\right) \quad (9)$$

where θ_{re} is the electrical rotor position, L_A represents the parameter of the inductance, which is independent of the electrical rotor position, and L_B represents the amplitude of the cosine component of the inductance. Note that the values in (4)–(9) will vary depending on different rotor positions. Further, the term L_q in (1)–(3) can be written as

$$L_q = L_{\mathrm{ls}} + \frac{3}{2}\left(L_A - L_B\right) \quad (10)$$

where L_{ls} is the leakage inductance. Given (1)–(3), three extended back-EMFs of the SynRM can be defined as

$$e_a = \frac{d}{dt}\left(L_{\mathrm{AA}} i_a + L_{\mathrm{AB}} i_b + L_{\mathrm{AC}} i_c\right) \tag{11}$$

$$e_b = \frac{d}{dt}\left(L_{\mathrm{BA}} i_a + L_{\mathrm{BB}} i_b + L_{\mathrm{BC}} i_c\right) \tag{12}$$

$$e_c = \frac{d}{dt}\left(L_{\mathrm{CA}} i_a + L_{\mathrm{CB}} i_b + L_{\mathrm{CC}} i_c\right). \tag{13}$$

Substituting (11)–(13) into (1)–(3), respectively, one can obtain

$$v_z = r_s i_z + L_q \frac{d}{dt} i_z + e_z, \quad z \in \{a, b, c\}. \tag{14}$$

Given the a-b-c to $\alpha - \beta$ coordinate transformation, the stator voltages in the $\alpha - \beta$ reference frame can be rewritten as

$$\begin{bmatrix} v_\alpha \\ v_\beta \end{bmatrix} = \frac{1}{3}\begin{bmatrix} 2 & -1 & -1 \\ 0 & \sqrt{3} & -\sqrt{3} \end{bmatrix}\begin{bmatrix} v_a \\ v_b \\ v_c \end{bmatrix} \tag{15}$$

where v_α and v_β are the stator voltages on the $\alpha - \beta$ reference frame, respectively. Based on (14) and (15), two equivalent stator-voltage equations in the $\alpha - \beta$ reference frame can be obtained as

$$v_\alpha = r_s i_\alpha + L_q \frac{d}{dt} i_\alpha + e_\alpha \tag{16}$$

$$v_\beta = r_s i_\beta + L_q \frac{d}{dt} i_\beta + e_\beta \tag{17}$$

where $i_{\alpha,\beta}$ and $e_{\alpha,\beta}$ are the currents and extended back-EMFs on the $\alpha - \beta$ reference frame, respectively. Substituting (4)–(9) into (11)–(13) and using (14) and (15), one can obtain the extended back-EMFs e_α and e_β as

$$e_\alpha = \frac{d}{dt}\left\{L_B\left(3 i_a \cos\theta_{\mathrm{re}} + \sqrt{3}\left(i_b - i_c\right)\sin\theta_{\mathrm{re}}\right)\cos\theta_{\mathrm{re}}\right\} \tag{18}$$

$$e_\beta = \frac{d}{dt}\left\{L_B\left(3 i_a \cos\theta_{\mathrm{re}} + \sqrt{3}\left(i_b - i_c\right)\sin\theta_{\mathrm{re}}\right)\sin\theta_{\mathrm{re}}\right\}. \tag{19}$$

As can be seen from (18) and (19), e_α and e_β are composed of sine functions, cosine functions, electrical rotor positions, and stator currents rendering them highly nonlinear.

III. Model-Based Predictive Current Control

In this study, a voltage-source inverter is connected to the SynRM as shown in Fig. 1, where V_{dc} is the dc-link voltage, and $\mathrm{G}_1 - \mathrm{G}_6$ are the six switches of the inverter. The eight different conducting modes of the inverter, denoted as $S_0 - S_7$, are listed in Table I. The relationship between the output voltages and the conduction mode is given in Table II. The discrete-time version corresponding to (16) and (17) in the $\alpha - \beta$ reference frame can be expressed as

$$v_x(k) = r_s i_x(k) + \frac{L_q}{T_s}\left(i_x(k+1) - i_x(k)\right) + e_x(k), \quad x \in \{\alpha, \beta\} \tag{20}$$

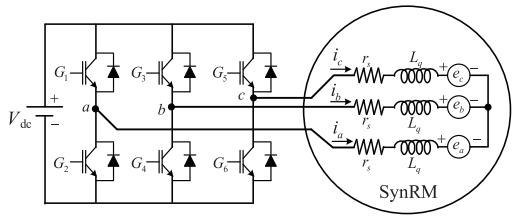

Fig. 1. Six-switching three-phase inverter connected to a SynRM.

TABLE I
Conducting Modes of Six-Switch Three-Phase Inverter

	Conducting modes							
	S_0	S_1	S_2	S_3	S_4	S_5	S_6	S_7
Switches on	G_2, G_4, G_6	G_1, G_4, G_6	G_2, G_3, G_5	G_2, G_3, G_6	G_1, G_4, G_5	G_2, G_4, G_5	G_1, G_3, G_6	G_1, G_3, G_5
Switches off	G_1, G_3, G_5	G_2, G_3, G_5	G_1, G_4, G_6	G_1, G_4, G_5	G_2, G_3, G_6	G_1, G_3, G_6	G_2, G_4, G_5	G_2, G_4, G_6

TABLE II
Relationship Between Conducting Mode and Output Voltages

Conducting mode	Output voltages				
	v_a	v_b	v_c	v_α	v_β
S_0	0	0	0	0	0
S_1	$2V_{dc}/3$	$-V_{dc}/3$	$-V_{dc}/3$	$2V_{dc}/3$	0
S_2	$-2V_{dc}/3$	$V_{dc}/3$	$V_{dc}/3$	$-2V_{dc}/3$	0
S_3	$-V_{dc}/3$	$2V_{dc}/3$	$-V_{dc}/3$	$-V_{dc}/3$	$\sqrt{3}\,V_{dc}/3$
S_4	$V_{dc}/3$	$-2V_{dc}/3$	$V_{dc}/3$	$V_{dc}/3$	$-\sqrt{3}\,V_{dc}/3$
S_5	$-V_{dc}/3$	$-V_{dc}/3$	$2V_{dc}/3$	$-V_{dc}/3$	$-\sqrt{3}\,V_{dc}/3$
S_6	$V_{dc}/3$	$V_{dc}/3$	$-2V_{dc}/3$	$V_{dc}/3$	$\sqrt{3}\,V_{dc}/3$
S_7	0	0	0	0	0

where the subscript "X" denotes the α-axis or the β-axis, $v_x(k)$ is the (k)th sampled stator voltage, $e_x(k)$ is the (k)th sampled extended back-EMF, T_s is the sampling interval, and $i_x(k)$ and $i_x(k+1)$ are the (k)th and $(k+1)$th sampled stator currents, respectively.

Given (20), the (k)th extended back-EMF can be expressed as

$$e_x(k) = v_x(k) - r_s i_x(k) - \frac{L_q}{T_s}\left(i_x(k+1) - i_x(k)\right). \tag{21}$$

Based on (21), it is not difficult to obtain the following $(k+1)$th sampled stator current:

$$i_x(k+1) = \left(1 - \frac{r_s T_s}{L_q}\right) i_x(k) + \frac{T_s}{L_q}\left(v_x(k) - e_x(k)\right). \tag{22}$$

In the (k)th sampling period, the (k)th extended back-EMF $e_x(k)$ cannot be calculated using (21) because of the appearance of the future value $i_x(k+1)$. The following approximation resolves that difficulty [5], [6]:

$$e_x(k) \approx e_x\left(k-1\right) \tag{23}$$

provided that the sampling interval T_s is sufficiently short. Fortunately, the latter condition holds thanks to the modern microprocessor technologies. Although (23) is not a perfect

solution, it is a simple yet effective way to estimate the (k)th extended back-EMF using its previous value. Following (21), the $(k+1)$th extended back-EMF can be expressed as

$$e_x(k+1) = v_x(k+1) - r_s i_x(k+1) - \frac{L_q}{T_s}\left(i_x(k+2) - i_x(k+1)\right). \tag{24}$$

According to (24), the $(k+2)$th sampled stator current can be obtained as

$$i_x(k+2) = \left(1 - \frac{r_s T_s}{L_q}\right) i_x(k+1) + \frac{T_s}{L_q}\left(v_x(k+1) - e_x(k+1)\right). \tag{25}$$

Using the MBPCC with delay compensation from [6], one may express the current prediction of (25) as

$$i_x^p(k+2)|_{S_0,\ldots,S_7} = \left(1 - \frac{r_s T_s}{L_q}\right) i_x^p(k+1) + \frac{T_s}{L_q}\left(v_x(k+1)|_{S_0,\ldots,S_7} - \hat{e}_x(k+1)\right) \tag{26}$$

where the superscripts "p" and "$\wedge$" refer to the predicted and estimated values, respectively. Given (22), the predicted current $i_x^p(k+1)$ appearing in (26) can be replaced by

$$i_x^p(k+1) = \left(1 - \frac{r_s T_s}{L_q}\right) i_x(k) + \frac{T_s}{L_q}\left(v_x(k) - \hat{e}_x(k)\right). \tag{27}$$

The combination of (21) and (23) naturally leads to the following (k)th estimated back-EMF

$$\hat{e}_x(k) = v_x(k-1) - r_s i_x(k-1) - \frac{L_q}{T_s}\left(i_x(k) - i_x(k-1)\right). \tag{28}$$

Likewise, the $(k+1)$th estimated back-EMF will be written as

$$\hat{e}_x(k+1) = v_x(k) - r_s i_x(k) - \frac{L_q}{T_s}\left(i_x^p(k+1) - i_x(k)\right). \tag{29}$$

Next, define the following cost function to evaluate the current errors between the commands and the predictions

$$g(k)|_{S_0,\ldots,7} = \left|i_\alpha^*(k+2) - i_\alpha^p(k+2)|_{S_0,\ldots,7}\right| + \left|i_\beta^*(k+2) - i_\beta^p(k+2)\right|_{S_0,\ldots,7}\Big| \tag{30}$$

where the superscript "$*$" refers to the reference command. Based on a second-order extrapolation [8], the current references $i_\alpha^*(k+2)$ and $i_\beta^*(k+2)$ can be approximated by

$$i_\gamma^*(k+2) = 6\cdot i_\gamma^*(k) - 8\cdot i_\gamma^*(k-1) + 3\cdot i_\gamma^*(k-2), \quad \gamma \in \{\alpha, \beta\}. \tag{31}$$

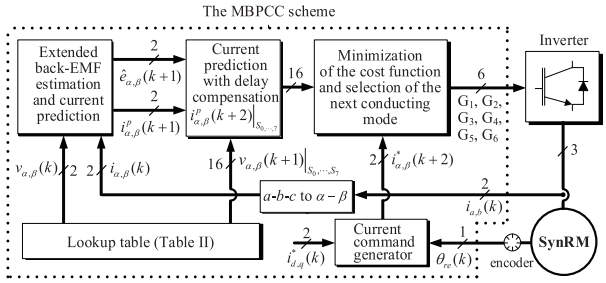

Fig. 2. MBPCC scheme of the SynRM drive system.

TABLE III
PARAMETERS OF A SYNRM

r_s, Ω	2.5
L_A, mH	12
L_B, mH	8
L_{ls}, mH	10
L_q, mH	16
L_d, mH	40

As can be seen from Table II, there are eight different possible conducting modes, each of which corresponds to a pair of output voltages, which yields a predicted current value depicted by (26). According to (30), an optimal conducting mode S_l can be determined by

$$g(k)|_{S_l \in \{S_0,\ldots,S_7\}} = \min\left\{g(k)|_{S_0}, \ldots, g(k)|_{S_7}\right\}. \tag{32}$$

The MBPCC scheme is shown in Fig. 2, where $i_{d,q}^*(k)$ refers to the current command in the d–q reference frame, and the number attached to each arrow represents the number of different inputs. Using the d–q to $\alpha-\beta$ coordinate transformation and (31), one may obtain the current reference $i_{\alpha,\beta}^*(k+2)$. The conducting mode S_l satisfying (32) then will be adopted to control the six switches $G_1 - G_6$ of the drive system in the $(k+1)$th sampling period. As can be observed from Fig. 2, no PWM technique is used to control the inverter.

IV. Improved Model-Free Predictive Current Control

Theoretically, the stator current of the three-phase decoupled load can be predicted by MBPCC [5], [6] with satisfactory accuracy if the used model and parameters are ideal. However, for the SynRM, it is impossible to obtain its true parameter values and back-EMFs appearing in (16) and (17) in practice. A fixed set of parameters in (26) and Table III will produce considerable current prediction errors due to the fact that parameter variations would occur under a wide range of operating conditions, along with the fact that the estimation errors associated with the back-EMFs would always exist. It is desired that the dependence on parameters and back-EMFs be eliminated, motivating the development of a model-free approach. The principle of the model-free approach has been successfully applied to sensorless controls [22], [24], [25]. Following that spirit, the present work attempts to realize the MFPCC [17] on the SynRM drive system.

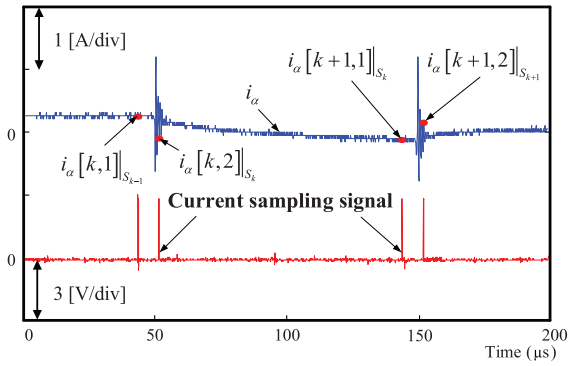

Fig. 3. Current detections performed twice based on MFPCC [17].

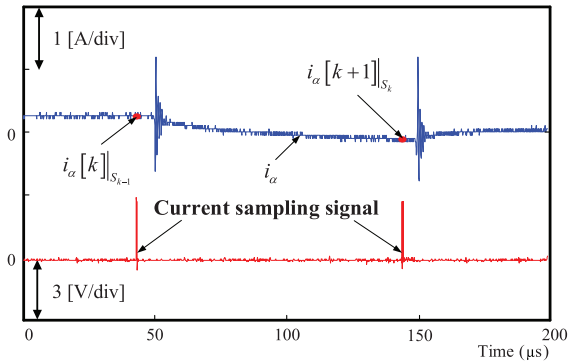

Fig. 4. Current detection performed once based on proposed IMFPCC.

Recall that in [17], two current measurements (here labeled as "1" and "2," respectively) are required in each sampling period, which may result in the detection of current spikes, as shown in Fig. 3. To prevent this from happening, a common practice is to delay the second current detection for a fixed amount of time after applying a conducting mode. However, the choice of a suitable delay time depends largely on experience and the inverter's characteristics. In a worst case, a bad choice of delay time from unexperienced users may result in damage to the drive systems. As there is no general guideline regarding the choice of delay time, a reliance on experience may hinder the popularization of MFPCC, which may in turn limit its applicability and practicality. To permanently resolve the issue aforementioned, a single current detection method is proposed in this paper. In each sampling period, the current detection is performed immediately before a conducting mode is applied, as shown in Fig. 4.

Another drawback of MFPCC [17] is the stagnant current-variation update, meaning that certain conducting modes may not have been used after dozens of consecutive sampling intervals. The current variation corresponding to a conducting mode in [17] is updated once in every sampling period. It cannot rule out that the above-mentioned stagnant update problem will not occur, which may significantly reduce the current-prediction accuracy. A solution is proposed to resolve this problem.

The principle of IMFPCC is illustrated in Fig. 5, which shows the possible current trajectories under different conducting modes. To avoid a current spike, it is worth noting that the α-axis stator current is measured before the new conducting mode is applied in each sampling period.

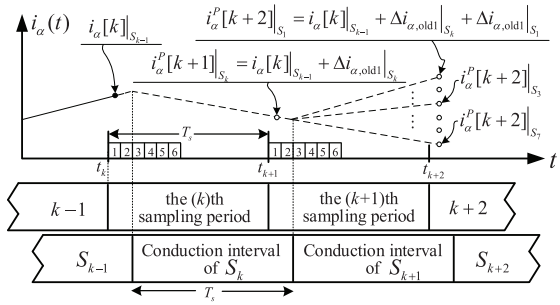

1: Measure stator current
2: Output new switching state
3: Calculate and update old current variation
4: Estimate current variation
5: Compute current command
6: Execute current prediction, calculate cost, and choose next switching state

Fig. 5. Schematic representation of the proposed current-prediction method.

In Fig. 5, the (k)th sampled α-axis stator current under the conducting mode $S_{k-1} \in \{S_0, \ldots, S_7\}$ is denoted as $i_\alpha[k]|_{S_{k-1}}$. In the same figure, $i_\alpha^P[k+2]|_{S_1}$, $i_\alpha^P[k+2]|_{S_3}$, $i_\alpha^P[k+2]|_{S_7}$, and $i_\alpha^P[k+1]|_{S_k}$ represent the predicted α-axis stator currents under the conducting modes S_1, S_3, S_7, and $S_k \in \{S_0, \ldots, S_7\}$, respectively. Similar to $i_\alpha[k]|_{S_{k-1}}$, the future currents $i_\alpha[k+1]|_{S_k}$ and $i_\alpha[k+2]|_{S_{k+1}}$ under the conducting modes S_k and $S_{k+1} \in \{S_0, \ldots, S_7\}$ will be measured in the $(k+1)$th and $(k+2)$th sampling periods, respectively. Using an add-and-subtract technique, one can easily obtain the following equation:

$$i_\alpha[k+2]|_{S_{k+1}} = i_\alpha[k]|_{S_{k-1}} + \left(i_\alpha[k+1]|_{S_k} - i_\alpha[k]|_{S_{k-1}}\right) + \left(i_\alpha[k+2]|_{S_{k+1}} - i_\alpha[k+1]|_{S_k}\right). \quad (33)$$

For convenience, two current variations in (33) are defined as follows:

$$\Delta i_\alpha|_{S_k} = i_\alpha[k+1]|_{S_k} - i_\alpha[k]|_{S_{k-1}} \quad (34)$$

$$\Delta i_\alpha|_{S_{k+1}} = i_\alpha[k+2]|_{S_{k+1}} - i_\alpha[k+1]|_{S_k}. \quad (35)$$

In the (k)th sampling period, the two current variations $\Delta i_\alpha|_{S_k}$ and $\Delta i_\alpha|_{S_{k+1}}$ cannot be measured because of the unavailability of the future currents $i_\alpha[k+1]|_{S_k}$ and $i_\alpha[k+2]|_{S_{k+1}}$ appearing in (34) and (35), respectively. Fortunately, their previous values can be used in this case as substitutes because any two neighboring current variations under the same conducting modes are close to each other, provided the sampling interval T_s is fixed and sufficiently short [17]. Throughout this study, the sampling interval of the 100-MHz TMS320F2809 microprocessor (made by Texas Instruments) is set to 100μs [17]. Both algorithms, the MBPCC and the IMFPCC, work well under this setting. Evidently, a shorter sampling interval can be achieved if a faster microcontroller is used, which could reduce the prediction errors further. Below are two expressions that can be used to approximate (34) and (35), respectively

$$\Delta i_\alpha|_{S_k} \approx \Delta i_{\alpha,\text{old1}}|_{S_k \in \{S_0,\ldots,S_7\}} \quad (36)$$

$$\Delta i_\alpha|_{S_{k+1}} \approx \Delta i_{\alpha,\text{old1}}|_{S_{k+1} \in \{S_0,\ldots,S_7\}} \quad (37)$$

where the subscript "old1" refers to previous current variations stored in the microprocessor.

Considering the left-hand side of (39), its previous value will be backed up and denoted with the subscript "old2" as follows:

$$\Delta\, i_{\alpha,\text{old2}}\big|_{S_l\in\{S_0,\ldots,S_7\}} = \Delta\, i_{\alpha,\text{old1}}\big|_{S_l=S_{k-1}}. \tag{38}$$

As $S_{k-1}\in\{S_0,\ldots,S_7\}$, there are eight values in (38) that will be backed up to check the existence of conducting mode stagnation. To reduce the approximation errors in (36) and (37), the following update mechanism is adopted to refresh the current variations:

$$\Delta\, i_{\alpha,\text{old1}}\big|_{S_{k-1}\in\{S_0,\ldots,S_7\}} = i_\alpha[k]\big|_{S_{k-1}} - i_\alpha[k-1]\big|_{S_{k-2}}. \tag{39}$$

Note that the update speed of (39) is very fast because of the high-performance microprocessor, and the left-hand side of (39) assumes eight different values under eight different conducting modes, as listed in Table I. In principle, a higher sampling frequency yields better accuracy for the approximated current variations. Given (33)–(39), together with Fig. 5, the predicted α-axis stator current under the conducting mode S_j can be calculated as follows:

$$i_\alpha^P[k+2]\big|_{S_j} = i_\alpha[k]\big|_{S_{k-1}} + \Delta\, i_{\alpha,\text{old1}}\big|_{S_k} + \Delta\, i_{\alpha,\text{old1}}\big|_{S_j} \tag{40}$$

with the superscript "P" denoting the predicted value. Following the above procedures, one can obtain the predicted β-axis stator current as

$$i_\beta^P[k+2]\big|_{S_j} = i_\beta[k]\big|_{S_{k-1}} + \Delta\, i_{\beta,\text{old1}}\big|_{S_k} + \Delta\, i_{\beta,\text{old1}}\big|_{S_j}. \tag{41}$$

As there are eight different conducting modes, there will also be eight current predictions for the α- and β-axes, respectively. Note that the backup values of (38) will not be used in (40) and (41). Next, a cost function associated with the conducting mode S_j is defined as

$$\begin{aligned} g[k]\big|_{S_j} = &\left|i_\alpha^*[k+2] - i_\alpha^P[k+2]\big|_{S_j}\right| \\ &+ \left|i_\beta^*[k+2] - i_\beta^P[k+2]\big|_{S_j}\right| \end{aligned} \tag{42}$$

where the superscript "*" represents the current command. Given (31), the current commands $i_\alpha^*[k+2]$ and $i_\beta^*[k+2]$ can be calculated. In the (k)th sampling period, (42) yields eight cost values. A conducting mode S_m is selected, which gives the minimum cost value, i.e.,

$$g[k]\big|_{S_m\in\{S_0,\ldots,S_7\}} = \min\left\{g[k]\big|_{S_0},\ldots,g[k]\big|_{S_7}\right\}. \tag{43}$$

The model is avoided based on the following two assumptions. 1) The sampling interval of digital signal processor (DSP) is short enough, e.g., 100 μs or shorter. 2) The two current variations differ very little if a conducting mode is applied at two different time instants that are very close. Equations (36) and (37), describing current variations, hold under these two assumptions, and based on which current prediction then becomes possible, as depicted by (40) and (41), leading naturally to the model-free approach. In addition, as shown in (40) and (41), the current predictions are based on the sampled currents and the calculated current variations. The stator currents of the SynRM can be measured precisely by current sensors. In addition, current variations are updated in a very short time period, which is achieved by the DSP with a high sampling frequency. In contrast to the MBPCC using (26)–(29), the IMFPCC using (40) and (41) does not use any parameters or the back-EMF estimations.

If the value of (39) corresponding to one conducting mode is not refreshed during several dozens of time intervals, the stagnant conducting mode may negatively affect the current-prediction accuracies found in (40) and (41), and this is one shortcoming of [17]. For this reason, a simple solution is proposed here as shown in Fig. 6, where $g_{\min}$ and S_m are variables that stand for the minimum value and the corresponding optimal conducting mode, satisfying (43); r is the time-interval count. In this study, $\bar{r}$ is set to 50.

If a conducting mode $S_l\in\{S_0,\ldots,S_7\}$ has not been applied after 50 successive sampling intervals, S_m will be replaced by S_l in the next sampling interval. Following (44), the stagnant update detection is performed once every 50 sampling intervals, which does not require much computational overhead

$$S_m = S_l, \quad \text{if } \Delta\, i_{\alpha,\text{old2}}\big|_{S_l} = \Delta\, i_{\alpha,\text{old1}}\big|_{S_l} \text{ and } r=\bar{r}. \tag{44}$$

If (44) does not hold, then the optimal conducting mode S_m will be determined by (43). In other words, the stagnant conducting mode will be detected by (44) for $l=0,\ldots,7$. In summary, the conducting mode S_m chosen from (43) and (44) will be applied in the $(k+1)$th sampling period to control the inverter. The block diagram of the proposed IMFPCC is shown in Fig. 7, where $i_d^*[k]$ and $i_q^*[k]$ denote the $d-$ and q-axes current commands, and $\theta_{re}[k]$ represents the rotor position. Note that there is no need for any kind of PWM technique or linear regulator.

V. Simulation Results

Numerical simulations are carried out using MATLAB 2014a software and its Simulink tool to compare the performance of the IMFPCC against that of the MBPCC. In the simulations, the sampling interval is chosen to be 100 μs, the motor's speed command is chosen as 500 r/min, the q-axis current command is generated by a proportional-integral (PI)-based speed controller, and the d-axis current command is fixed as 1 A. Once the d- and q-axes current commands are determined, the α- and β-axes current commands can be obtained accordingly.

The nominal parameters of the motor are provided in Table III. To illustrate the effect of parameter variations on performance, the resistance and the q-axis inductance of the motor are, respectively, varied while the rest parameters are kept unchanged. To quantify the current-tracking performance, two mean absolute errors are defined as follows:

$$M_Y = \frac{1}{N}\sum_{k=1}^{N}|e_Y[k]| = \frac{1}{N}\sum_{k=1}^{N}|i_Y^*[k]-i_Y[k]|,\quad Y\in\{\alpha,\beta\} \tag{45}$$

$$\bar{M} = \frac{(M_\alpha+M_\beta)}{2} \tag{46}$$

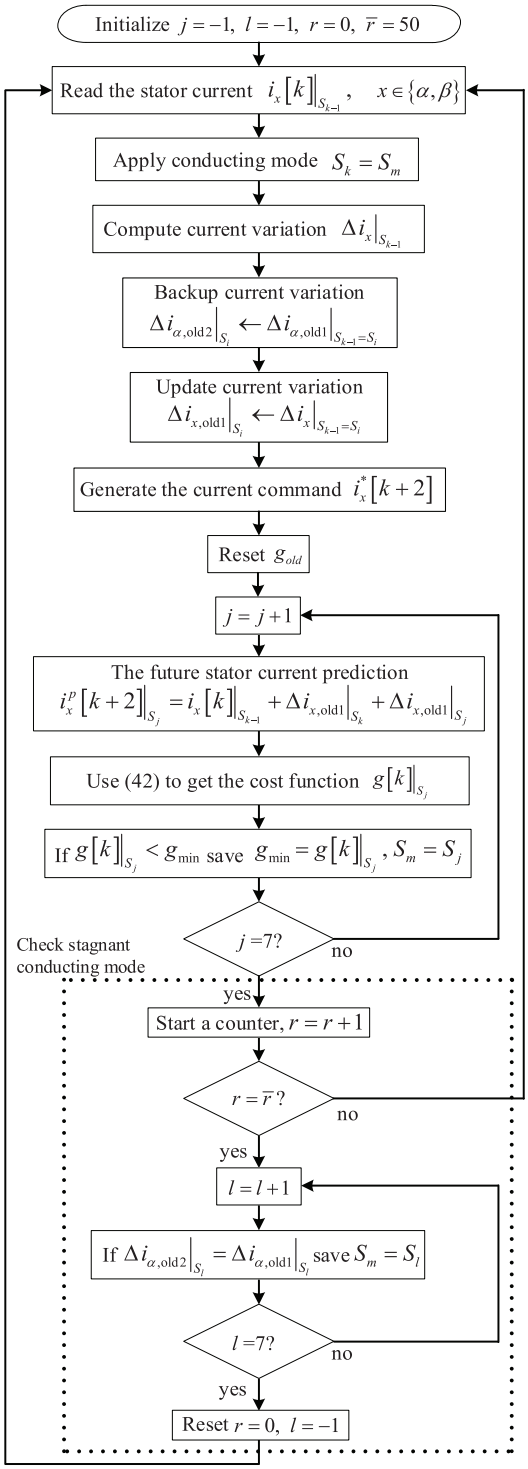

Fig. 6. Flowchart of the proposed IMFPCC.

where N is the total number of sampling points. Two alternative performance indexes in terms of current ripples are defined as

$$J_X=\sqrt{\frac{1}{N}\sum_{k=1}^{N}\left(i_X^*[k]-i_X[k]\right)^2},\quad X\in\{\alpha,\beta\} \tag{47}$$

$$\bar{J}=\frac{(J_\alpha+J_\beta)}{2}. \tag{48}$$

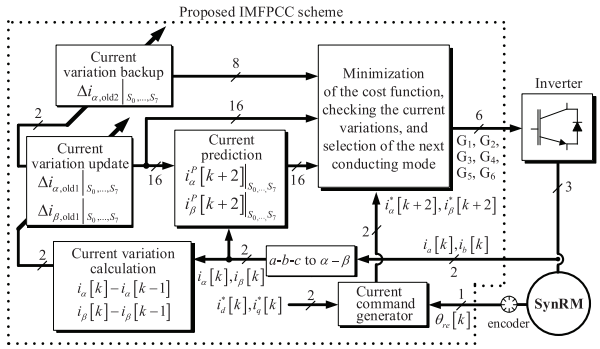

Fig. 7. Block diagram of the SynRM drive system with IMFPCC.

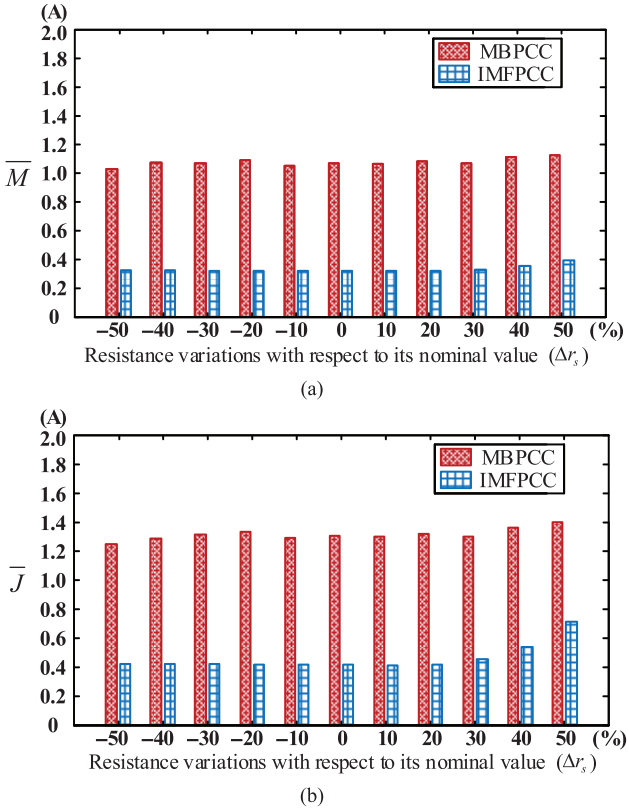

Fig. 8. Comparisons of the MBPCC and the IMFPCC under resistance variations based on performance indexes (a) $\bar{M}$ and (b) $\bar{J}$.

Fig. 8 shows the current tracking errors of MBPCC and IMFPCC, where $\bar{M}$ and $\bar{J}$ are defined in (46) and (48), respectively. In Figs. 8 and 9, the values of resistance and inductance are varied from -50% to $+50\%$ with respect to their nominal ones. Theoretically, the IMFPCC is insensitive to parameter variations. However, since the gains of the PI-based speed controller are fixed in the simulations, the corresponding q-axis current commands will vary if the motor parameters are changed, ranging from -50% to 50% with respect to the nominal values in this case. As a result, the current errors calculated through (45) to (48) will be affected, which can be observed from Figs. 8 and 9. For the IMFPCC, its current variations corresponding to the eight conducting modes will be refreshed automatically following (39). In contrast to that, the parameters of the MBPCC, as in (26)–(29), are fixed and never updated

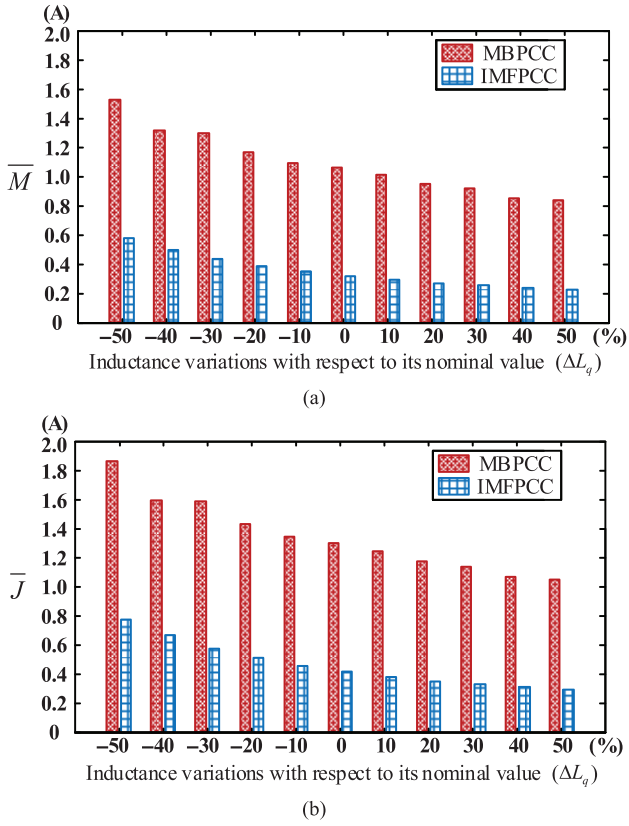

Fig. 9. Comparisons of the MBPCC and the IMFPCC under q-axis inductance variations based on performance indexes (a) $\bar{M}$ and (b) $\bar{J}$.

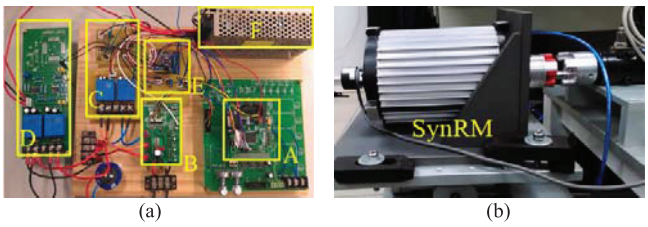

Fig. 10. SynRM drive system. (a) Drive circuit. (b) SynRM.

due to its nature. Consequently, the current errors of the former are smaller than that of the latter, as can be seen from Figs. 8 and 9.

VI. Experimental Results

Some experiments are conducted to validate the proposed IMFPCC and verify its feasibility whose results are shown in Figs. 11–17. In addition, the MBPCC is implemented for performance comparison purpose, and both of them are realized through a Texas Instruments microprocessor TMS320F2809. The two algorithms are programmed by Code Composer Studio (CCS) in *C Language*, and will be executed within the sampling period of 100 μs. The parameters of a prototyped SynRM, used in (26)–(30) for the MBPCC, are as follows: $L_q = 16$ mH, $r_s = 2.5\ \Omega$, and $T_s = 100$ μs. Two photo pictures of the drive circuit and the SynRM are provided in Fig. 10(a) and (b), respectively. As can be seen from Fig. 10(a), the drive circuit consists of six parts. Part A is a microprocessor development

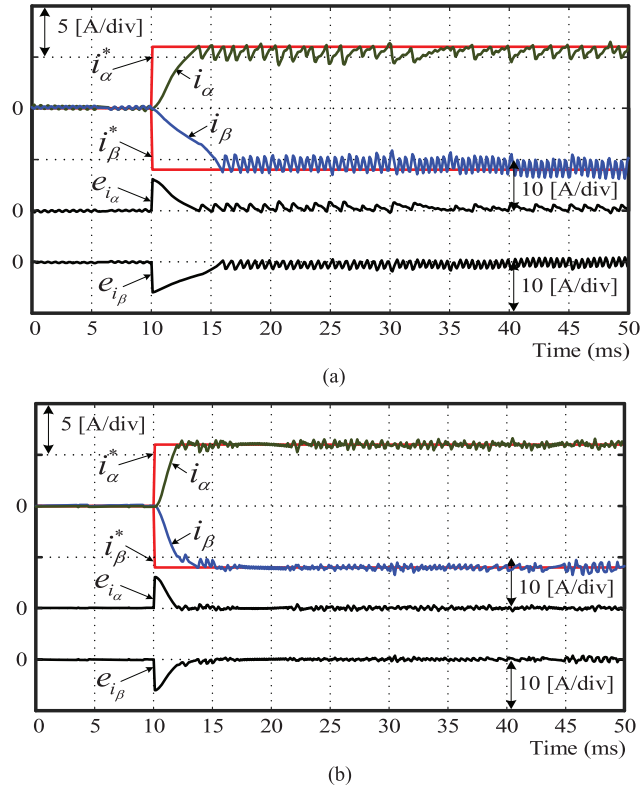

Fig. 11. Experimental results showing the current responses of (a) MBPCC and (b) proposed IMFPCC. The current commands of the α- and β-axes change from 0 to 6 A and 0 to -6A at 10 ms, respectively.

board containing the chip TMS320F2809, of which the maximum frequency is 100 MHz. Part B is an inverter power module SCM1246MF made by the Sanken Electric Company. This power module includes six insulated-gate bipolar transistors (IGBTs) with a 600-V breakdown voltage and a 30-A continuous rating current. Part C is the current sensing circuit, including two LA-25NP sensors made by LEM. Part D is a voltage-sensing circuit with two LV-25P sensors made by LEM. Part E is a low-cost analog-to-digital converter AD7655 featuring four channels and 16-bit resolution. Part F is a power supply.

Fig. 11 shows the current responses of the two methods, where i_α^* and i_β^* refer to the α- and β-axes current commands, respectively, i_α and i_β stand for the α- and β-axes currents, respectively, in which the current errors are defined as $e_{i_\alpha} = i_\alpha^* - i_\alpha$ and $e_{i_\beta} = i_\beta^* - i_\beta$. Note that in Fig. 11(a) and (b), the α- and β-axes current commands suddenly change from 0 to 6 A and 0 to -6 A at 10 ms, respectively. Compared to the results of MBPCC as shown in Fig. 11(a), a faster current response and smaller current ripples are obtained using the proposed IMFPCC as shown in Fig. 11(b). The current responses and their corresponding tracking errors as well as the speed response under a low-speed operation at 50 r/min are shown in Fig. 12, where ω_{rm} is the rotor speed. Fig. 13(a) and (b) shows the results when the motor is operated at 500 r/min. Note that the rotor speeds, shown in Figs. 12 and 13, are regulated by the same PI-based controller.

Figs. 12(b) and 13(b) reveal that the proposed IMFPCC has much better current-tracking performance in yielding smaller

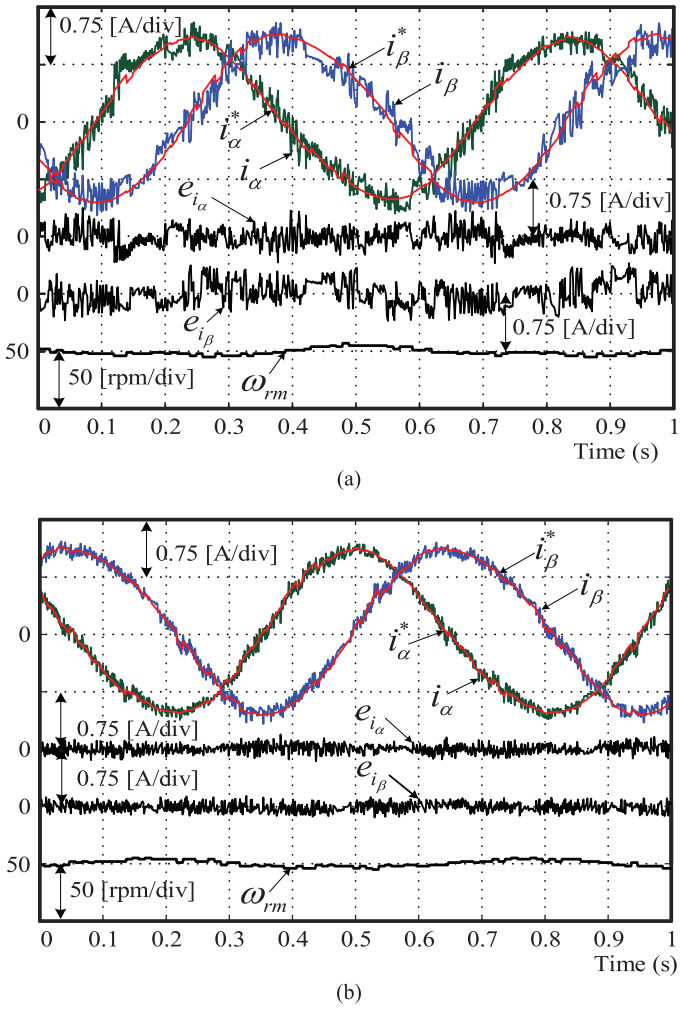

Fig. 12. Experimental results showing the current responses, the current errors, and the speed response of (a) MBPCC and (b) proposed IMFPCC with the SynRM operated at 50 r/min.

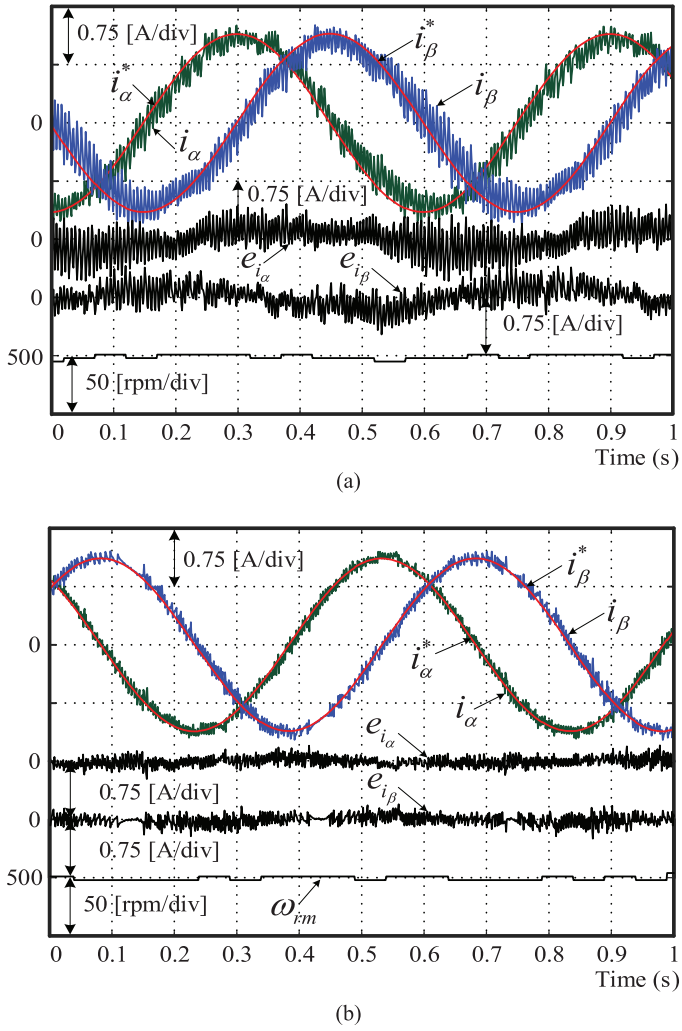

Fig. 13. Experimental results showing the current responses, the current errors, and the speed response of (a) MBPCC and (b) proposed IMFPCC with the SynRM operated at 500 r/min.

current errors, compared to that of the MBPCC as shown in Figs. 12(a) and 13(a) when the motor is operated at two constant speeds of 50 and 500 r/min, respectively. Figs. 14 –17 present experimental results of the two PCC schemes regarding their dynamic performance. Fig. 14 shows the current responses and the corresponding errors with current commands changing sequentially at 0.05, 0.1, and 0.15 s, respectively. In the same figure, both PCC schemes can control the real currents reaching the corresponding current commands. Even though both methods can achieve their current control objectives, Fig. 14(b) illustrates that the proposed IMFPCC has superior tracking performance in comparison with that of the MBPCC as shown in Fig. 14(a). Figs. 15 and 16 present the test results of the two PCC methods subject to sinusoidal current commands whose amplitudes change abruptly from 1 to 6 A at 0.2 s. With respect to Fig. 15(a), the current-tracking performance of the IMFPCC, as shown in Fig. 16(a), is largely improved, achieving a satisfactory transient response and following the current commands very well. Figs. 15(b) and 16(b) show the current trajectories and their corresponding errors in the $\alpha - \beta$ stationary coordinates. There are two circles on the left-hand side of Figs. 15(b) and 16(b), representing the current trajectories. The small circle and the large one show the current trajectories with the amplitudes of sinusoidal current commands set to 1 and 6 A, respectively. Note that the line connecting the two circles in Figs. 15(b) and 16(b) represents the transient trajectory. Clearly, as can be seen from Figs. 15 and 16, the proposed IMFPCC outperforms the MBPCC in the steady-state and the transient responses. Similar results can be observed from Fig. 17, where the current command i^*_α changes abruptly from -5 to 5 A at 0.1 s. As for the performance of command following, the IMFPCC displays fast current transition and smaller current ripples, as can be observed from Fig. 17. Fig. 17(a) and (b) shows that the transition of the α-axis current from -5 to 5 A does not affect that of the β-axis during the period from 0.08 to 0.12 s. Along with the simulation results, these experimental results demonstrate that the proposed IMFPCC has better current-tracking capability. One may, therefore, conclude that the proposed IMFPCC controls the stator currents of the SynRM more effectively than the MBPCC does.

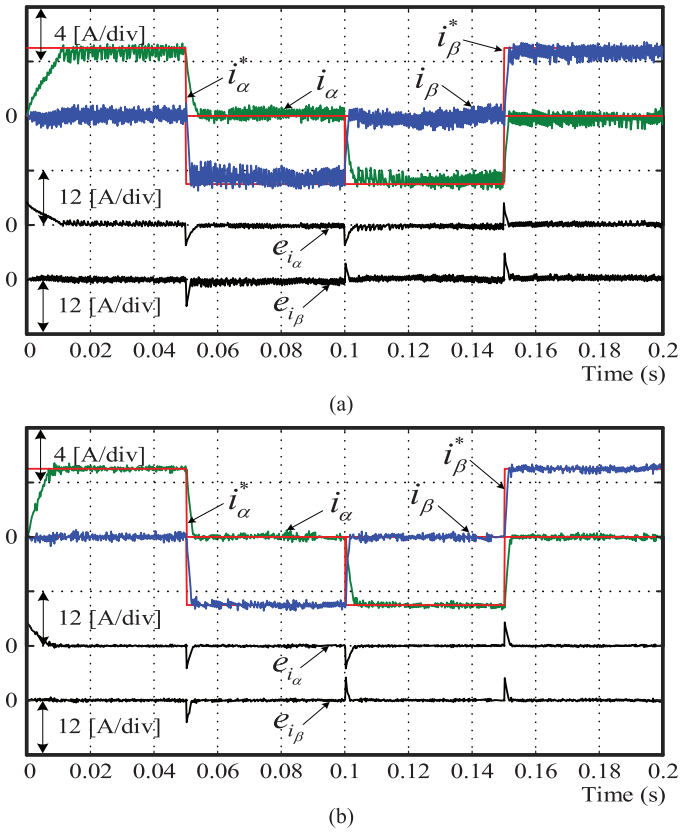

Fig. 14. Experimental results showing the current responses and the current errors of (a) MBPCC and (b) proposed IMFPCC. The current command of the α-axis changes sequentially from 5 to 0 A, 0 to -5 A, and -5 to 0 A at 0.05, 0.1, and 0.15 s, respectively, whereas the current command of the β-axis changes from 0 to -5 A, -5 to 0 A, and 0 to 5 A at 0.05, 0.1, and 0.15 s, respectively.

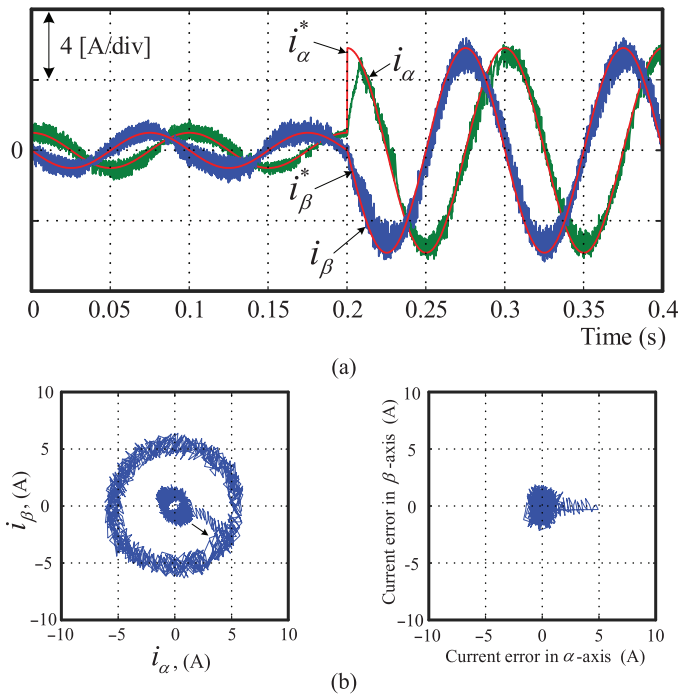

Fig. 15. Experimental results of the MBPCC scheme with amplitudes of sinusoidal current commands changing from 1 to 6 A at 0.2 s. (a) Current responses. (b) Current trajectory (left) and current error trajectory (right) in the $\alpha - \beta$ stationary coordinates, respectively.

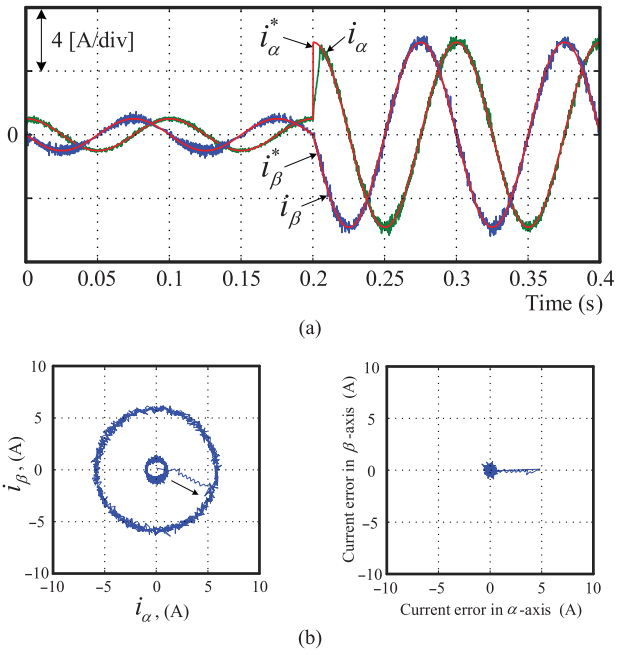

Fig. 16. Experimental results of the proposed IMFPCC scheme with amplitudes of sinusoidal current commands changing from 1 to 6 A at 0.2 s. (a) Current responses. (b) Current trajectory (left) and current error trajectory (right) in the $\alpha - \beta$ stationary coordinates, respectively.

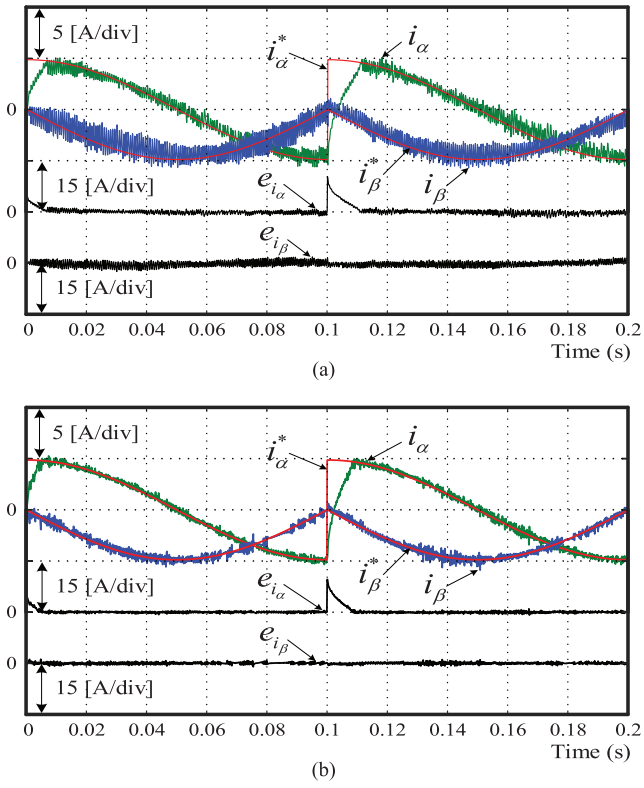

Fig. 17. Experimental results showing the current responses and the current errors of (a) MBPCC and (b) proposed IMFPCC. The α-axis current command changes from -5 to 5 A abruptly at 0.1 s.

VII. Conclusion

In this paper, an IMFPCC was proposed and successfully applied to a SynRM drive system through a microprocessor TMS320F2809. The contributions of the proposed IMFPCC

lie in two major respects. 1) It reduced the number of current measurement in each sampling period from two to one avoiding the detection of current spikes existed in previous MFPCC method. 2) It devised a new update mechanism which eliminated successfully stagnant conduction mode occurred in MFPCC. Moreover, it removes the restrictions of the MBPCC, which relies on the knowledge of motor parameters, back-EMFs, and stator voltages. As the proposed IMFPCC does not involve any multiplication operation, the computational burden of the corresponding algorithm is, compared to MBPCC, much lower making it quite suitable for realization. The proposed method retains all benefits of the MBPCC, i.e., neither the PWM nor the linear regulator is required, hence providing an appealing solution to control the current of SynRM. Simulation and experimental results illustrate that the proposed IMFPCC outperforms the MBPCC in yielding better and satisfactory transient as well as steady-state current responses.

Acknowledgment

The authors would like to thank the reviewers for their constructive suggestions, which greatly improved this paper.

References

[1] D. M. Brod and D. W. Novotny, "Current control of VSI-PWM inverters," *IEEE Trans. Ind. Appl.*, vol. IA-21, no. 3, pp. 562–570, May/Jun. 1985.
[2] M. Kazmierkowski, R. Krishnan, and F. Blaabjerg, *Control in Power Electronics*. New York, NY, USA: Academic, 2002.
[3] X. Li, S. Dusmez, B. Akin, and K. Rajashekara, "A new SVPWM for the phase current reconstruction of three-phase three-level T-type converters," *IEEE Trans. Power Electron.*, vol. 31, no. 3, pp. 2627–2637, Mar. 2016.
[4] H. A. Young, M. A. Perez, J. Rodriguez, and H. Abu-Rub, "Assessing finite-control-set model predictive control: A comparison with a linear current controller in two-level voltage source inverters," *IEEE Ind. Electron. Mag.*, vol. 8, no. 1, pp. 44–52, Mar. 2014.
[5] J. Rodriguez *et al.*, "Predictive current control of a voltage source inverter," *IEEE Trans. Ind. Electron.*, vol. 54, no. 1, pp. 495–503, Feb. 2007.
[6] P. Cortes, J. Rodriguez, C. Silva, and A. Flores, "Delay compensation in model predictive current control of a three-phase inverter," *IEEE Trans. Ind. Electron.*, vol. 59, no. 2, pp. 1323–1325, Feb. 2012.
[7] M. Rivera, V. Yaramasu, A. Llor, J. Rodriguez, B. Wu, and M. Fadel, "Digital predictive current control of a three-phase four-leg inverter," *IEEE Trans. Ind. Electron.*, vol. 60, no. 11, pp. 4903–4912, Nov. 2013.
[8] P. M. Sanchez, O. Machado, E. J. B. Peña, F. J. Rodriguez, and F. J. Meca, "FPGA-based implementation of a predictive current controller for power converters," *IEEE Trans. Ind. Informat.*, vol. 9, no. 3, pp. 1312–1321, Aug. 2013.
[9] J. Scoltock, T. Geyer, and U. K. Madawala, "A model predictive direct current control strategy with predictive references for MV grid-connected converters with LCL-filters," *IEEE Trans. Power Electron.*, vol. 30, no. 10, pp. 5926–5937, Oct. 2015.
[10] M. Rivera *et al.*, "Review of predictive control methods to improve the input current of an indirect matrix converter," *IET Power Electron.*, vol. 7, no. 4, pp. 886–894, Apr. 2014.
[11] B. S. Riar, T. Geyer, and U. K. Madawala, "Model predictive direct current control of modular multilevel converters: Modeling, analysis, and experimental evaluation," *IEEE Trans. Power Electron.*, vol. 30, no. 1, pp. 431–439, Jan. 2015.
[12] Y. Zhang and H. Yang, "Two-vector-based model predictive torque control without weighting factors for induction motor drives," *IEEE Trans. Power Electron.*, vol. 31, no. 2, pp. 1381–1390, Feb. 2016.
[13] J. Hong, D. Pan, and Z. Zong, "Comparison of the two current predictive-control methods for a segment-winding permanent-magnet linear synchronous motor," *IEEE Trans. Plasma Sci.*, vol. 41, no. 5, pp. 1167–1173, May 2013.
[14] S. Carpiuc and C. Lazar, "Fast real-time constrained predictive current control in permanent magnet synchronous machine-based automotive traction drives," *IEEE Trans. Transport. Electrif.*, vol. 1, no. 4, pp. 326–335, Dec. 2015.
[15] C. Xia, Y. Wang, and T. Shi, "Implementation of finite-state model predictive control for commutation torque ripple minimization of permanent-magnet brushless dc motor," *IEEE Trans. Ind. Electron.*, vol. 60, no. 3, pp. 896–905, Mar. 2013.
[16] A. Darba, F. De Belie, P. D'haese, and J. A. Melkebeek, "Improved dynamic behavior in BLDC drives using model predictive speed and current control," *IEEE Trans. Ind. Electron.*, vol. 63, no. 2, pp. 728–740, Feb. 2016.
[17] C.-K. Lin, T.-H. Liu, J. Yu, L.-C. Fu, and C.-F. Hsiao, "Model-free predictive current control for interior permanent-magnet synchronous motor drives based on current difference detection technique," *IEEE Trans. Ind. Electron.*, vol. 61, no. 2, pp. 667–681, Feb. 2014.
[18] W. Xu, "Novel decoupling model-based predictive current control strategy for flux-switching permanent-magnet synchronous machines with low torque ripple and switching loss," *IEEE Trans. Appl. Superconduct.*, vol. 24, no. 5, pp. 1–5, Oct. 2014.
[19] H. Guzman, F. Barrero, and M. J. Duran, "IGBT-gating failure effect on a fault-tolerant predictive current-controlled five-phase induction motor drive," *IEEE Trans. Ind. Electron.*, vol. 62, no. 1, pp. 15–20, Jan. 2015.
[20] P. Cortes, M. P. Kazmierkowski, R. M. Kennel, D. E. Quevedo, and J. Rodriguez, "Predictive control in power electronics and drives," *IEEE Trans. Ind. Electron.*, vol. 55, no. 12, pp. 4312–4324, Dec. 2008.
[21] C.-K. Lin, L.-C. Fu, T.-H. Liu, and C.-F. Hsiao, "Passivity-based adaptive complementary PI sliding-mode speed controller for synchronous reluctance motor using predictive current control," in *Proc. Amer. Control Conf.*, Jun. 2012, pp. 1168–1173.
[22] M.-Y. Wei and T.-H. Liu, "A high-performance sensorless position control system of a synchronous reluctance motor using dual current-slope estimating technique," *IEEE Trans. Ind. Electron.*, vol. 59, no. 9, pp. 3411–3426, Sep. 2012.
[23] M.-Y. Wei, T.-H. Liu, and C.-K. Lin, "Design and implementation of a passivity-based controller for sensorless synchronous reluctance motor drive systems," *IET Elect. Power Appl.*, vol. 5, no. 4, pp. 335–349, Apr. 2011.
[24] J.-L. Shi, T.-H. Liu, and Y.-C. Chang, "Position control of an interior permanent-magnet synchronous motor without using a shaft position sensor," *IEEE Trans. Ind. Electron.*, vol. 54, no. 4, pp. 1989–2000, Jun. 2007.
[25] M.-T. Lin and T.-H. Liu, "Sensorless synchronous reluctance drive with standstill starting," *IEEE Trans. Aerosp. Electron. Syst.*, vol. 36, no. 4, pp. 1232–1241, Oct. 2000.

Cheng-Kai Lin was born in Taipei, Taiwan, on July 11, 1980. He received the B.S. degree in electrical engineering from Ming Chi University of Technology, Taipei, Taiwan, in 2002, and the M.S. and Ph.D. degrees in electrical engineering from National Taiwan University of Science and Technology, Taipei, Taiwan, in 2004 and 2009, respectively.

From October 2009 to August 2012, he was a Postdoctoral Researcher with the Department of Electrical Engineering, National Taiwan University, Taipei, Taiwan. He is currently an Assistant Professor of Electrical Engineering with National Taiwan Ocean University, Keelung, Taiwan. His research interests include motor drive control, power electronic applications, and control applications.

Jen-te Yu received two M.S. degrees, one in aerospace engineering and another in electrical engineering from Wichita State University, Wichita, KS, USA, and Georgia Institute of Technology, Atlanta, GA, USA, respectively, and the Ph.D. degree in electrical engineering from National Taiwan University, Taipei, Taiwan.

He is currently a Postdoctoral Researcher with the Department of Electrical Engineering, National Taiwan University. His research interests include the areas of multi-agent systems, nonlinear control, motion control, robust control, and optimal control.

Yen-Shin Lai (M'96–SM'01–F'14) received the M.S. degree from National Taiwan University of Science and Technology, Taipei, Taiwan, in 1987, and the Ph.D. degree from the University of Bristol, Bristol, U.K., in 1995, both in electronic engineering.

In 1987, he joined the Department of Electrical Engineering, National Taipei University of Technology, Taipei, Taiwan, where he served as the Chairperson during 2003–2006, and has been a Full Professor since 1999, a Distinguished Professor since 2006, and a Chair Professor since 2013. His research interests include control of power converters, inverters, and motor drives.

Dr. Lai is currently the Chair of the Electrical Power Engineering Division, Ministry of Science and Technology, Taiwan, and a Vice President of the Taiwan Power Electronics Association.

Hsing-Cheng Yu (M'13) was born in Hsinchu, Taiwan, on November 14, 1977. He received the M.S. and Ph.D. degrees in mechanical engineering from National Chiao Tung University, Hsinchu, Taiwan, in 2002 and 2010, respectively.

He is currently an Assistant Professor with the Department of Systems Engineering and Naval Architecture, National Taiwan Ocean University, Keelung, Taiwan. His research interests include motor design and drive control, optomechatronics system integration, and ocean energy systems.